

Enhancing Material Boundary Visualizations in 2D Unsteady Flow through Local Reference Frame Transformations

Xingdi Zhang¹  and Peter Rautek¹  and Thomas Theußl¹  and Markus Hadwiger¹ 

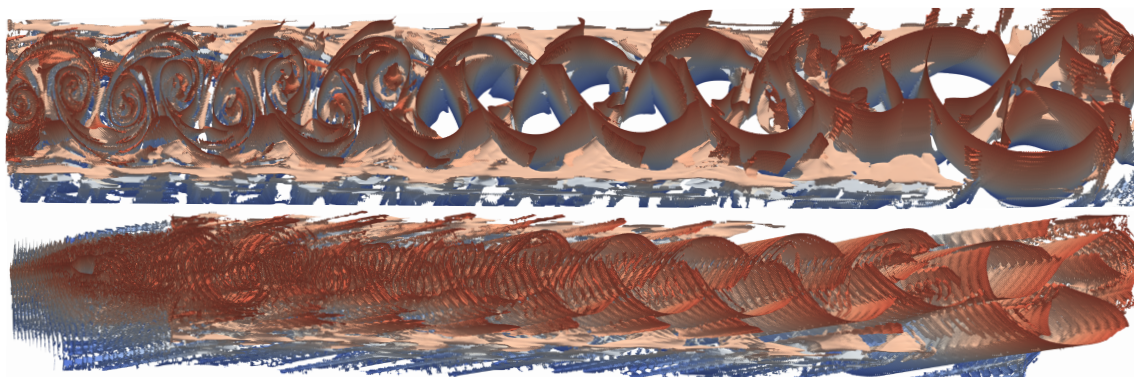


Figure 1: Material boundaries of a vortex street computed as FTLE ridges in $(2+1)$ -D space-time. A key advantage of our framework is that it allows using standard algorithms and software components for efficient and accurate feature extraction. Here, the ridge surfaces in space-time were extracted using ParaView: (Top) Both feature extraction and visualization done in a reference frame moving with the vortex street. (Bottom) The same algorithms in the input (lab) reference frame become significantly less accurate, harder to interpret, and take longer to compute.

Abstract

We present a novel technique for the extraction, visualization, and analysis of material boundaries and Lagrangian coherent structures (LCS) in 2D unsteady flow fields relative to local reference frame transformations. In addition to the input flow field, we leverage existing methods for computing reference frames adapted to local fluid features, in particular those that minimize the observed time derivative. Although, by definition, transforming objective tensor fields between reference frames does not change the tensor field, we show that transforming objective tensors, such as the finite-time Lyapunov exponent (FTLE) or Lagrangian-averaged vorticity deviation (LAVD), or the second-order rate-of-strain tensor, into local reference frames that are naturally adapted to coherent fluid structures has several advantages: (1) The transformed fields enable analyzing LCS in space-time visualizations that are adapted to each structure; (2) They facilitate extracting geometric features, such as iso-surfaces and ridge lines, in a straightforward manner with high accuracy. The resulting visualizations are characterized by lower geometric complexity and enhanced topological fidelity. To demonstrate the effectiveness of our technique, we measure geometric complexity and compare it with iso-surfaces extracted in the conventional reference frame. We show that the decreased geometric complexity of the iso-surfaces in the local reference frame, not only leads to improved geometric and topological results, but also to a decrease in computation time.

CCS Concepts

• **Human-centered computing** → Visualization; • **Applied computing** → Physical sciences and engineering;

1 Introduction

Understanding the dynamics of fluid motion in 2D unsteady flow fields is important for both theoretical exploration and practical applications. Methods relying on the visualization of fluid flow by directly showing the paths of individual particles face significant challenges due to the inherent instability and sensitivity of Lagrangian fluid motion to initial conditions. This complexity necessitates the development of robust techniques that can reveal the underlying structures governing fluid dynamics beyond the behavior of single particles. Among these techniques, the identification and

analysis of Lagrangian coherent structures (LCS) have emerged as a cornerstone for a deeper understanding of fluid motion. LCS, as investigated in early work by Haller and Yuan [HY00], serve as the backbone of Lagrangian fluid dynamics by highlighting the most repelling, attracting, and shearing material surfaces. These structures are pivotal in simplifying the overall geometry of the flow, providing precise quantification of material transport, and offering insights about major flow features and mixing processes [Hal15].

Building upon this foundational understanding, our work introduces a novel approach to enhance the computation, visualization,

and analysis of Lagrangian material boundaries in 2D unsteady flow fields. By exploiting local reference frame transformations, which either explicitly minimize the observed time derivative [HMTR19] or are known to co-move with important features, we are effectively transforming objective scalar fields, such as finite-time Lyapunov exponent (FTLE) or Lagrangian-averaged vorticity deviation (LAVD) fields into a local reference frame corresponding to the LCS. This transformation allows us to present LCS and their material boundaries in a frame of reference that simplifies computations and visual analysis. Flow features observed in the lab frame can shift substantially between consecutive time steps, causing iso-surface extraction methods to inadvertently merge or split surfaces and thus distort their topology. In contrast, a co-moving local frame keeps features nearly stationary across time steps, preserving more accurate iso-surfaces.

The contributions of our method are twofold. Firstly, we contribute to the field of fluid dynamics visualization by showcasing the effectiveness of direct visualizations of Lagrangian coherent structures (LCS) in locally-adapted reference frames. Secondly, we show that the extraction of iso-surfaces and other geometric features, such as ridge lines, in their local reference frames, results in smoother geometries in space-time as well as enhanced topological fidelity. This, in turn, opens up new avenues for research and application, including the potential for improved prediction and manipulation of fluid behavior in various scientific and engineering contexts. While we build on an extensive amount of previous work, we for the first time bring together the computation of reference frames with the computation and visualization of coherent structures and the corresponding material boundaries in an interactive framework. One key advantage of our proposed method is that the computation of iso-surfaces in their local reference frames can be done by standard algorithms and software components. We demonstrate that the computation of iso-surfaces in the local reference frame using VTK [Kit03, SML06], not only results in triangle meshes with lower complexity and less topological artifacts, but also in lower computation times.

2 Related Work

Feature extraction in fluid flow is a long-standing important topic in continuum mechanics as well as in visualization. See, e.g., the state of the art report by Post et al. [PVH*03], or the feature flow fields of Theisel et al. [TS03]. Very powerful general approaches for feature extraction and tracking have been presented, such as in the feature tracking kit (FTK) [GLX*21]. This often involves determining a well-adapted space-time mesh, including recent work such as that of Ren and Guo [RG23]. One key advantage of our approach is that simple reference frame transformations can sometimes help reduce the need for more complicated approaches such as feature-adapted meshes. In a suitably transformed field, we can make use of existing implementations based on regular grids (e.g., VTK [Kit03, SML06], ParaView [AGL05], or the Topology toolkit [TFL*17, BMBF*19]). Defining and finding features is often done on the basis of topological properties and structures. See the state of the art report on topology-based visualization of unsteady flow by Pobitzer et al. [PPF*10], the early work of Perry and Chong [PC87, PC94], or recent work on the distinguished hyperbolic trajectories for 2D time-dependent vector field topology of Hofmann and Sadlo [HS20].

Lagrangian coherent structures (LCS) Coherent structures have long been considered to be important topics in flow visualiza-

tion, see, e.g., Kasten et al. [KWP*10]. A well-known definition of LCS was introduced by Haller and Yuan [HY00], with an approachable introduction by Haller [Hal15]. Serra [Ser17] provides an in-depth overview of Eulerian and Lagrangian objective structures and their applications. Lagrangian transport phenomena in geophysical flows are very important, see, e.g., Jones and Winkler [JW02].

Finite-time Lyapunov exponents (FTLE). One option to compute LCS as distinguished material surfaces is to build on FTLE fields, as proposed by Haller [Hal01], in which LCS are defined as ridges of FTLE fields [SLM05]. Ridges have, for example, been extracted with the Marching Ridges algorithm [FP01] as implemented in the VCG ParaView plugins [SHH*19]. This has been used for visualizing LCS extracted as ridges from FTLE fields by Sadlo and Peikert [SP09], for example.

Reference frame transformations and invariance. The invariance of physical computations with respect to the chosen *reference frame* or *observer* is an important topic in continuum mechanics and visualization. Earlier work often focused on Galilean invariance [Lug79, SWH05, WSTH07, BHJ16]. It is, however, often seen as important to not only be indifferent to equal-speed translations of the reference frame, but also with respect to arbitrary rotations of the frame. Together, invariance with respect to all rigid reference frame motions (translations, rotations) is referred to as *objectivity* [Ast79, DL76, Ogd97, TN65] in both fluid mechanics [Hal05, HHHF16] and visualization research [GST16, HMTR19, THR*21]. Other proposed types of invariance include rotation invariance [GST16], similarity and affine invariance [GT20], and invariance under displacement transformations [BRG20].

Fluid properties can be computed in a way that *by construction* is objective. For example, the observation of the vorticity tensor in the eigenbasis of the rate-of-strain tensor [DL76, Ast79], using the strain acceleration tensor [Hal05], or observing instantaneous vorticity deviations and averages along particle trajectories (path lines) [HHFH16] (LAVD). Moreover, the observation of hyperbolic stretching behavior computed via the finite-time Lyapunov exponent (FTLE) [SLM05, HY00]. In fluid mechanics, objective concepts have been established for all three kinds of Lagrangian coherent structures [Hal15], i.e., parabolic, elliptic, and hyperbolic LCS.

Alternatively, a special reference frame can be determined in an objective manner via optimization, which then makes other originally non-objective properties objective if they are computed in this optimal frame. The first approach that proposed this idea was presented by Günther et al. [GGT17], who formulated the search for the optimal observer as a linear optimization that minimizes the unsteadiness of the observed flow field. This can also be formulated in terms of the observed time derivative defined by Hadwiger et al. [HMTR19]. The approach by Günther et al. [GGT17] and its extensions [GT20, BRG20, THR*21] perform reference frame optimization completely locally. A global optimization scheme was proposed by Hadwiger et al. [HMTR19], which was also extended to curved spaces by Rautek et al. [RMB*21]. These optimization techniques can be the basis for subsequent interactive exploration of reference frames and flow fields, as shown by Zhang et al. [ZHTR22]. An optimal reference frame can also be computed locally in a manner that is guided by user interaction, such as the *vortex lens* metaphor proposed by Rautek et al. [RZW*24].

Other optimization methods can also be used to optimally observe objective properties, such as computing the objective deformation component of a velocity field as proposed Kaszás et al. [KPH22], who compute the reference frame that minimizes the observed kinetic energy of the flow field. Another fruitful avenue is using machine learning methods for robust reference frame extraction, as shown by Kim and Günther [KG19]. Apart from objective vortex extraction [GT18], reference frame considerations have also been important in the development of unsteady vector field topology [BYH*20].

Vortex detection. A particularly important coherent structure are vortices. See the state of the art report on vortex extraction by Günther and Theisel [GT18], in which computational methods are categorized as either region-based or line-based. Well-known examples for region-based methods include the criteria of Okubo [Oku70], Weiss [Wei91], Hunt [HWM88], and Jeong and Hussain [JH95]. Examples for line-based methods are Sujudi and Haimes [SH95], the computation of feature flow fields for critical points [TS03], the parallel vectors operator of Peikert and Roth [PR99], and tracking of swirling stream lines [BP02, TWHS05, TWSH02]. The LAVD field by Haller et al. [HHFH16] facilitates detecting vortices both as regions as well as a vortex core line located at the isolated maximum of the LAVD scalar field. Other vortex detection methods include those based on vector field decomposition [BPKB14], the geometric method by Xie et al. [XXLL10], the integration based methods by Globus et al. [GLL91], using the acceleration magnitude as Kasten et al. [KRHH11], the approach by Wiebel et al. [WCW*09] or Sadlo et al. [SPP04], the predictor-corrector method by Banks and Singer [BS95], and vortex boundary detection using machine learning methods [BCG20].

3 Mathematical Framework

In this section, we rigorously define reference frames, their transformations, and key related concepts used throughout this paper. The flow domain is a manifold M , specifically $M = \mathbb{R}^2$ for 2D unsteady flow fields $\mathbf{v}(x, t)$, with $x \in \mathbb{R}^2$. Reference frames are described infinitesimally as (Killing) vector fields $\mathbf{w}(x, t)$ on M .

3.1 Reference Frames

Because any reference frame by itself can only be given explicitly relative to *some* other reference frame, it is customary to define a reference frame via the *transformation* between two reference frames. In order to transform between two frames, we define a time-dependent family of diffeomorphisms $t \mapsto \phi_t$. For fixed time t , each diffeomorphism ϕ_t is a smooth map with smooth inverse from the manifold M to itself, and $t \mapsto \phi_t$ depends smoothly on the time parameter t . That is, we have

$$\begin{aligned} \phi_t : M &\rightarrow M, \\ y &\mapsto \phi_t(y) =: x. \end{aligned} \quad (1)$$

This should be interpreted as points labeled x representing spatial points (actual points, not x coordinates) in the original (input) reference frame (often also called the lab frame), and spatial points labeled y representing points (actual points, not y coordinates) in the reference frame that we want to transform to. We will also simply say frame x or frame y . Fig. 2 depicts space-time visualizations for both frames.

For physically-realizable observers, each diffeomorphism ϕ_t must be an isometry [ZHTR22]. For $M = \mathbb{R}^2$ (or \mathbb{R}^3), these isometries can be given as

$$\phi_t(y) = w(t) + \mathbf{Q}(t)(y - w(t_0)). \quad (2)$$

Here, $w(t_0)$ is some arbitrary position at time $t = t_0$; each $\mathbf{Q}(t)$ is a rotation tensor (i.e., a proper orthogonal tensor, meaning it has determinant 1.0, and $\mathbf{Q}^T(t)\mathbf{Q}(t) = \mathbf{I}$, and $\mathbf{Q}(t_0) = \mathbf{I}$ (identity)).

We can therefore also define a reference frame as a map

$$t \mapsto (w(t), \mathbf{Q}(t)). \quad (3)$$

The map $t \mapsto w(t)$ determines a space-time curve which we call a *world line*, and $t \mapsto \mathbf{Q}(t)$ is a time-dependent rotation. Both maps $w(t)$ and $\mathbf{Q}(t)$ are chosen to be smooth with respect to time, and we can therefore compute the time derivatives $\dot{w}(t)$ and $\dot{\mathbf{Q}}(t)$ of both functions.

3.2 Reference Frames as Time-Dependent Killing fields

Instead of only working with translations and rotations as above, it is beneficial to work with the derivatives of reference frame transformations, which are given by velocity fields that are Killing vector fields [HMTR19]. Killing fields are the derivatives of isometries, also called *infinitesimal isometries*. One immediate benefit that arises from this is that all Killing fields on a manifold form a vector space (of vector fields), whose dimensionality is the number of degrees of freedom of an infinitesimal reference frame transformation on the underlying manifold. This enables using linear combinations of linearly independent *basis Killing fields* in order to describe any reference frame [ZHTR22].

Given the map $t \mapsto \phi_t$ from Eq. 1, the vector field \mathbf{w} that describes the corresponding infinitesimal transformation is given by

$$\mathbf{w}(x, t) := \left. \frac{d}{d\tau} \right|_{\tau=t} \phi_\tau(y), \quad \text{with } y = \phi_t^{-1}(x). \quad (4)$$

When ϕ_t is an isometry, \mathbf{w} is a Killing field. Using Eq. 2, we obtain

$$\begin{aligned} \mathbf{w}(x, t) &= \left. \frac{d}{d\tau} \right|_{\tau=t} w(\tau) + \left. \frac{d}{d\tau} \right|_{\tau=t} \mathbf{Q}(\tau)(y - w(t_0)), \\ &= \dot{w}(t) + \dot{\mathbf{Q}}(t)(y - w(t_0)), \\ &= \dot{w}(t) + \mathbf{\Omega}(t)\mathbf{Q}(t)(y - w(t_0)), \quad \text{with } \mathbf{\Omega} := \dot{\mathbf{Q}}\mathbf{Q}^T, \\ &= \dot{w}(t) + \mathbf{\Omega}(t)(x - w(t)). \end{aligned} \quad (5)$$

For the last step, we have used $y = \phi_t^{-1}(x)$ with ϕ_t as in Eq. 2, giving

$$y = w(t_0) + \mathbf{Q}^T(t)(x - w(t)). \quad (6)$$

Most importantly, we have introduced the *anti-symmetric* spin tensor $\mathbf{\Omega}$, i.e., $\mathbf{\Omega} = -\mathbf{\Omega}^T$, determining the angular velocity of the frame y relative to the input frame x . We can now see that, according to the definition of Killing fields, the vector \dot{w} and the anti-symmetric tensor $\mathbf{\Omega}$ together uniquely define a Killing field on the manifold M . We also note that, for $M = \mathbb{R}^2$, \dot{w} has two degrees of freedom and $\mathbf{\Omega}$ has only one, while for $M = \mathbb{R}^3$ each of these has three degrees of freedom. Thus, in total we have exactly the dimensionality of the vector space of Killing fields as stated above.

Likewise, given a time-dependent vector field $\mathbf{w}(x, t)$, the time-dependent family of diffeomorphisms $\phi_t : M \rightarrow M$ is given by the

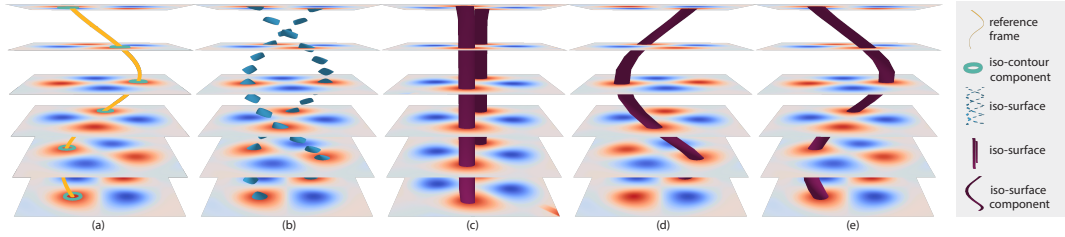


Figure 2: Discrete space-time structures. (a) Time slices (time depicted vertically) of discrete objective scalar field, world line $t \mapsto w(t)$ of reference frame (yellow), individual iso-contour components (cyan). (b) Iso-surfaces extracted in global input (lab) reference frame x . (c) Iso-surfaces extracted in the transformed space (determined by the time-dependent isometry ϕ_t) of the locally-determined reference frame y . (d) and (e) Two different iso-surface components transformed back (via the time-dependent inverse isometry ϕ_t^{-1}) into the original input (lab) frame x . Compare (b) with (c,d).

family of curves $t \mapsto \phi_t(y)$, for all $y \in M$, as solutions of the ODE

$$\frac{d}{dt} \phi_t(y) = \mathbf{w}(\phi_t(y), t). \quad (7)$$

To solve Eq. 7, we choose the initial values $\phi_{t_0}(y) = y$ for an arbitrary time t_0 , with the corresponding diffeomorphism ϕ_{t_0} the identity map.

Finally, from now on we will describe every reference frame as a Killing field \mathbf{w} on $M = \mathbb{R}^2$, referred to a basis of Killing fields \mathbf{e}_i as

$$\mathbf{w}(x, t) = a(t) \mathbf{e}_1(x) + b(t) \mathbf{e}_2(x) + c(t) \mathbf{e}_3(x), \quad a, b, c \in \mathbb{R}. \quad (8)$$

Without restriction of generality, we use the same basis fields \mathbf{e}_i as Zhang et al. [ZHTR22], given explicitly as follows. On the manifold $M = \mathbb{R}^2$, we use the following three linearly-independent basis Killing fields. The vectors $\mathbf{e}_i(x)$ ($i \in \{1, 2, 3\}$) at any spatial point $x = (\hat{x}, \hat{y}) \in \mathbb{R}^2$, using Cartesian coordinates (\hat{x}, \hat{y}) , are

$$\mathbf{e}_1(\hat{x}, \hat{y}) = \begin{bmatrix} 1 \\ 0 \end{bmatrix}, \quad \mathbf{e}_2(\hat{x}, \hat{y}) = \begin{bmatrix} 0 \\ 1 \end{bmatrix}, \quad \mathbf{e}_3(\hat{x}, \hat{y}) = \begin{bmatrix} 0 & -1 \\ 1 & 0 \end{bmatrix} \begin{bmatrix} \hat{x} \\ \hat{y} \end{bmatrix}. \quad (9)$$

For \mathbf{e}_3 , corresponding to input vector fields given on a rectangular domain $D = [x_a, x_b] \times [y_a, y_b] \subset \mathbb{R}^2$, with center point $(\hat{x}_0, \hat{y}_0) = \frac{1}{2}(x_a + x_b, y_a + y_b)$, we define coordinates $(\hat{x}, \hat{y}) := (\hat{x} - \hat{x}_0, \hat{y} - \hat{y}_0)$. Using these basis Killing fields, any Killing field (and, thus, infinitesimal reference frame motion) can be expanded using Eq. 8.

3.3 Locally Defining Reference Frames

Sec. 5 describes our approach for locally determining reference frames, which we simply refer to as local reference frame (LRF), in detail, and Sec. 6 describes how we use them to enhance visualization and analysis. However, to immediately expand on the above discussion, we briefly outline our options for defining reference frames locally:

1. We choose a spatial position, and extract a reference frame, given by $(a, b, c)(t)$, along the corresponding world line of an observer field \mathbf{u} (which is usually not a Killing field), as explained in detail by Zhang et al. [ZHTR22]. Because \mathbf{u} was computed to locally adapt to the flow field, the resulting reference frame is locally-adapted.
2. We extract a reference frame, given by $(a, b, c)(t)$, by using a local user interaction via the *vortex lens* of Rautek et al. [RZW*24]. Locality of the frame results from the locality of the vortex lens.
3. We extract a reference frame, given by $(a, b, c)(t)$, for a region $U \subset \mathbb{R}^2$. For example, we can compute the best L_2 fit of a Killing field to the flow in U , as done by Kaszás et al. [KPH22]. We can also use option 1 above to obtain a Killing field for each

point in U , and then from these compute the average Killing field for U . Locality immediately follows from the choice of region $U \subset \mathbb{R}^2$.

3.4 Objective Tensor Fields

A tensor field \mathbf{T} , of arbitrary order and type, including scalars and vectors, is *objective* if and only if under a frame change corresponding to the family of diffeomorphisms $t \mapsto \phi_t$ it transforms as

$$\mathbf{T}^* = \phi_t^* \mathbf{T}. \quad (10)$$

The notation ϕ_t^* denotes the *pullback* [O’N06] of the diffeomorphism $\phi_t: M \rightarrow M$ at fixed time t . The pullback connects points y with corresponding points $x = \phi_t(y)$, and, for Euclidean isometries (Eq. 6), it simply transforms vectors and linear maps of vectors by rotating them using combinations of \mathbf{Q} and \mathbf{Q}^T , as given explicitly below. In order for a tensor field to be objective, Eq. 10 must hold for all times t (i.e., for each t). In the following, the pullbacks are applied explicitly for different fields in $M = \mathbb{R}^2$ (also valid for \mathbb{R}^3).

Objective scalar fields. According to the above definition, a scalar field $f: M \rightarrow \mathbb{R}$ is objective if $f^* = \phi_t^* f$ holds. This means

$$f^*(y) = f(x), \quad \text{with } x = \phi_t(y). \quad (11)$$

Objective vector fields. A vector field \mathbf{v} is objective if $\mathbf{v}^* = \phi_t^* \mathbf{v}$ holds. Expanding the pullback of vector fields explicitly, this means

$$\mathbf{v}^*(y) = \mathbf{Q}^T \mathbf{v}(x), \quad \text{with } x = \phi_t(y). \quad (12)$$

Objective second-order tensor fields. A tensor field $\mathbf{S}: \mathbf{v} \mapsto \mathbf{S}(\mathbf{v})$ is objective if $\mathbf{S}^* = \phi_t^* \mathbf{S}$ holds. That is, expanding the pullback, if

$$\mathbf{S}^*(y) = \mathbf{Q}^T \mathbf{S}(x) \mathbf{Q}, \quad \text{with } x = \phi_t(y). \quad (13)$$

4 Objective Structures

Our interest focus on objective fluid structures – those independent of reference frame choice. Our primary targets are objective *space-time* structures, synthesized from objective Eulerian structures and Lagrangian (coherent) structures. While these structures are theoretically frame-invariant, can in principle be “extracted” in any reference frame, due to discretization and sampling the actual choice of reference frame for this computation can make a significant difference. See Figs. 2 and 3.

4.1 Objective Eulerian Structures

We define an objective Eulerian structure as a set of spatial points S_τ , for a fixed time $t = \tau$, where the way of determining this set of points

is independent of the chosen reference frame. That is, if we have any pair of reference frames x and y , as described above, then we must have

$$S_\tau(\text{frame-}x) = \phi_t(S_\tau(\text{frame-}y)). \quad (14)$$

This notation means that using the same way (algorithm, recipe; e.g., iso-contour extraction) of determining the set $S_\tau \subset \mathbb{R}^2$ independently in any of the two frames results in the same set of points, where “the same” is in the sense of the definition of the diffeomorphism ϕ_t in Eq. 1, mapping all points $y \in \mathbb{R}^2$ to the corresponding points $x \in \mathbb{R}^2$, at time t .

In particular, we are interested in objective Eulerian structures that are objective because they are *extracted* from objective tensor fields, for example by computing iso-contours of an objective scalar field $f: M \rightarrow \mathbb{R}$. An example for such an objective Eulerian scalar field is the *instantaneous vorticity deviation (IVD)* by Haller et al. [HHFH16]. We refer to the discussion of Mattia [Ser17] for more details and applications of *objective Eulerian coherent structures*.

4.2 Lagrangian Structures

Lagrangian structures often can be computed by integrating objective properties, such as an objective scalar field, along path lines [Ser17, HHHFH16]. As such, they are in essence objective by definition. However, it is crucial to note that this is only true if the integration in fact integrates an *objective* tensor field. Otherwise, the integration along path lines does not suddenly make a non-objective property objective.

Again, we are in particular interested in Lagrangian structures that are *extracted* from (integrated) objective tensor fields, for example by computing iso-contours of an objective scalar field $f: M \rightarrow \mathbb{R}$ that results from integration of an objective tensor field along path lines.

A very well-known example for such an objective Lagrangian scalar field is the *finite-time Lyapunov exponent fields (FTLE)* [Hal01, SLM05]. Another example is the *Lagrangian-Averaged Vorticity Deviation (LAVD)* defined by Haller et al. [HHFH16].

Lagrangian fields vs. Lagrangian coherent structures. A subtle point is that there is no single common definition of a Lagrangian coherent structure (LCS), and common definitions of LCS, e.g., [HY00, Hal15], do not necessarily fully coincide with the advection (under the flow map) of a Lagrangian scalar field such as FTLE [SLM05]. Because our focus is on the extraction and visualization of any such structure relative to local reference frames, we side-step this issue and for any particular user choice of a particular objective Lagrangian scalar field and its relation to a Lagrangian coherent structure we mainly defer to the user’s understanding and interpretation of that choice.

In Appendix A we describe the computation of objective tensor fields used in the examples of this paper.

4.3 Objective Space-Time Structures

We define an objective space-time structure for a fixed (finite) time interval $[t_0, t_1]$ to be a time-dependent set of points $S_{[t_0, t_1]}$, where the way of determining this set of points is, again, independent of the

chosen reference frame. That is, *any observer will determine the same set of points* $S_{[t_0, t_1]}$, where we analogously to Eq. 14 define

$$S_{[t_0, t_1]}(\text{frame-}x) = \phi_{[t_0, t_1]}(S_{[t_0, t_1]}(\text{frame-}y)). \quad (15)$$

With this notation we mean that, for the space-time structure $S_{[t_0, t_1]}$, Eq. 14 must hold for each fixed time t and the corresponding map ϕ_t .

4.4 Computation of Space-Time Structures

We now define a general function *Extract*, which takes an objective tensor field \mathbf{T} as input and produces an objective space-time structure $S_{[t_0, t_1]}$ as output. That is, we define the structure $S_{[t_0, t_1]}$ computed by

$$S_{[t_0, t_1]} := \text{Extract}(\mathbf{T}_{[t_0, t_1]}). \quad (16)$$

For tensor fields that are continuous in space and time, their extraction does not depend on the choice of observer, because of the frame-indifference of objective structures. Denoting a transformed tensor field by $\mathbf{T}_{[t_0, t_1]}^* = \phi_t^* \mathbf{T}_{[t_0, t_1]}$, as above, we thus know that the following equation must hold for any reference transformation ϕ_t :

$$\text{Extract}(\mathbf{T}_{[t_0, t_1]}^*) = \phi_{[t_0, t_1]}(\text{Extract}(\mathbf{T}_{[t_0, t_1]})). \quad (17)$$

However, if we now define an operator $\overline{\text{Extract}}$ that is a *discretized* version of the continuous operator *Extract*, we will, in general, have

$$\overline{\text{Extract}}(\mathbf{T}_{[t_0, t_1]}^*) \neq \phi_{[t_0, t_1]}(\overline{\text{Extract}}(\mathbf{T}_{[t_0, t_1]})). \quad (18)$$

We will in particular look at the problems incurred by discretizing the extraction operator *in time*. See Fig. 3 for an example.

5 Choosing Local Reference Frames

Our main goal is to work with a reference frame that is locally adapted to a Lagrangian structure of interest, as determined inter-

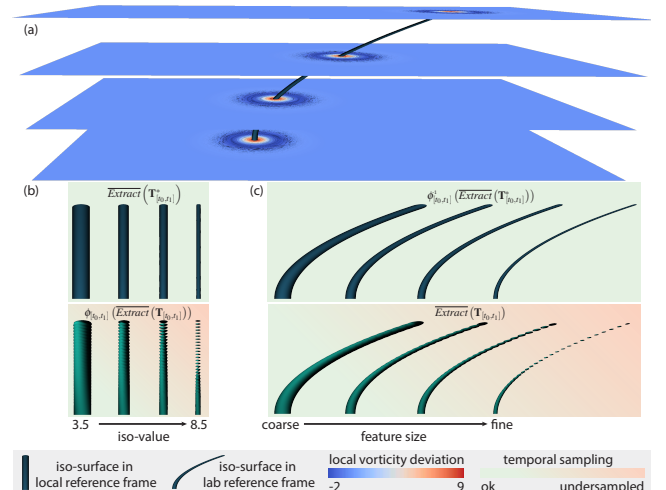


Figure 3: Temporal under-sampling of space-time structures. (a) Translating vortex with increasing translational speed. Iso-contour of local vorticity deviation extracted in local reference frame but visualized in lab reference frame. With faster translational speed as well as with finer detailed structures temporal under-sampling occurs in the lab reference frame. (b) and (c) Comparison of iso-surface extraction in local reference frame (blue surfaces), and in lab reference frame (green surfaces), visualized in (b) the local reference frame; and (c) the lab reference frame.

actively by the user. Visual guidance is provided by space-time visualizations, such as the ones in Fig. 2, for example by considering color-coded time slices of objective scalar fields such as LAVD or FTLE. Using this guidance, the user chooses a space-time point or region of interest, and then a reference frame corresponding to this user choice is either interactively *computed* (e.g., by using a vortex lens [RZW*24]), or *extracted* from a pre-computed observer field (e.g., as described by Zhang et al. [ZHTR22]). The observer field [HMTR19] used in the latter can be seen as containing infinitely many reference frames, one for each point in space, where each of these frames is locally adapted to the fluid flow around that point through the optimization process that was used to compute the observer field.

For most kinds of user interaction, we want the user to not only choose a reference frame interactively, but to also choose a specific world line $t \mapsto w(t)$ in the reference frame, as well as an iso-value for the surface extraction. The choice of reference frame, world line in that reference frame, and iso-value can be done by selecting a single space-time point for all three purposes. An example of this user interaction can be seen in the supplementary video.

To explain the difference between a reference frame and a specific world line, we would like to highlight a subtle point regarding Killing vector fields. From Eq. 3, we see that a specific world line can already be part of the definition of a reference frame. However, a Killing field is an entire vector field that is independent of any particular spatial point or world line—it is a vector field on the underlying manifold M , without any “special” point, just like the input vector field \mathbf{v} is. This fact can also be seen from Eq. 8, which is clearly independent of any particular point. In contrast, Eq. 5 ($\mathbf{w}(x, t) = \dot{w}(t) + \boldsymbol{\Omega}(t)(x - w(t))$) is another valid way of writing a Killing field, which happens to make use of a specific world line $w(t)$. But this definition results in the exact same vector space of Killing fields as Eq. 8, and the choice of world line $w(t)$ is *not* unique: For a specific Killing field, any world line can be used in Eq. 5 to define the same Killing field (corresponding to the exact same reference frame motion).

5.1 Choosing a Starting Point in Space-Time

The first main goal of user interaction with the input flow field is to choose a point in space-time, which determines a chosen start time (or reference time) t_0 and a corresponding spatial point $w(t_0)$. The user has the following options how to choose these

Direct selection of space-time point. The user selects a space-time point directly in a space-time visualization, such as the one shown in Fig. 2 (a). This point then is the point $w(t_0)$, at time t_0 .

Vortex lens selection. The user selects a space-time point to steer a *vortex lens*, and the selected point becomes the starting point for the vortex lens optimization described by Rautek et al. [RZW*24] to find the actual optimal point $w(t_0)$, taking into account the input field \mathbf{v} in the vortex lens region, in addition to the user’s initial chosen point.

Selection via iso-value. Considering a time slice with a color-coded objective scalar field, such as an objective vorticity deviation (IVD or LAVD), the user can select a space-time point to pick the corresponding scalar value as an *iso-value*. We then interactively

extract the corresponding iso-contour in the time slice that the user selected. Iso-contours often consist of multiple connected components, and we choose the component into which the user clicked and compute the centroid of that component. This point then becomes the selected space-time point for further interaction. It can be either (1) used directly, or (2) be used as the starting point for vortex lens optimization, as above.

5.2 Extracting a Local Reference Frame Transformation

In order to compute or extract a local reference frame, we have two main types of options: (1) We focus on a single space-time point, and extract a reference frame corresponding to that point. The main way of doing this is to use a pre-computed observer velocity field [GGT17, HMTR19, RMB*21, RZW*24]. However, focusing on a “single point” includes taking into account derivatives at that point, i.e., even in this case we mean a point and at least a small neighborhood around it. (2) We focus on a (potentially larger) region, over which a reference frame is computed, usually by minimizing a corresponding objective function. This region can be relatively large, as for example in Kaszás et al. [KPH22], or relatively small, as for example the vortex lens region in Rautek et al. [RZW*24].

5.2.1 Locality by choosing a space-time point

As above, by choosing a point we in fact mean choosing a point and its infinitesimal neighborhood around it, such that derivatives can be computed at the chosen point to take into account local flow properties.

Extraction from observer field. As described by Zhang et al. [ZHTR22], a very useful way to extract a local reference frame from an observer field \mathbf{u} is to let the user choose a space-time point, which we directly define as the starting point $w(t_0)$ at time t_0 . We then define the world line $t \mapsto w(t)$ by solving the ODE $\dot{w}(t) = \mathbf{v}(w(t), t)$ as

$$w(t) = w(t_0) + \int_{t_0}^t \mathbf{v}(w(\tau), \tau) d\tau. \quad (19)$$

The corresponding spin tensor is then determined by

$$\boldsymbol{\Omega}(t) = \frac{1}{2} \begin{bmatrix} \mathbf{0} & -\|\nabla \times \mathbf{u}(w(t), t)\| \\ \|\nabla \times \mathbf{u}(w(t), t)\| & \mathbf{0} \end{bmatrix}. \quad (20)$$

Together, the world line $t \mapsto w(t)$ and the spin tensor $\boldsymbol{\Omega}(t)$ now completely define the extracted reference frame as given by Eq. 5, i.e.,

$$\mathbf{w}(x, t) = \dot{w}(t) + \boldsymbol{\Omega}(t)(x - w(t)).$$

Extraction from input velocity field. A simple approach that can work well for simple flow fields with a well-chosen point $w(t_0)$ is to use the same recipe as above, but start from the field $\mathbf{u} := \mathbf{v}$, as also shown by Zhang et al. [ZHTR22]. This removes the need for the optimization of an observer field \mathbf{u} in a potentially costly pre-computation.

5.2.2 Locality by choosing a region

In addition to choosing a point (with an infinitesimal region around it), it can be beneficial to choose a region for which a reference frame is optimized. We use the region-based options described below.

Vortex lens interaction. The *vortex lens* described by Rautek et al. [RZW*24] lets the user interactively choose a space-time point and a lens region around it, and then interactively and progressively computes a reference frame that is adapted and optimized for the lens region.

Observed kinetic energy-minimizing reference frame. Translated to our terminology, Kaszás et al. [KPH22] propose to compute the Killing field \mathbf{w} that minimizes the kinetic energy of the input flow field in a region $U \subset \mathbb{R}^2$ transformed into the reference frame determined by the field \mathbf{w} . Computationally, they find the minimizer of

$$\min_{\mathbf{w}(t)} \int_{U(t)} \|\mathbf{v}(x,t) - \mathbf{w}(x,t)\|_2^2 dA. \quad (21)$$

The time-dependent field $\mathbf{w}(x,t)$ is computed for each time t separately, for which the above expression determines the field $\mathbf{w}(t)$ that is closest to the input field $\mathbf{v}(t)$ in the L_2 -norm, within a given region $U(t)$, and dA a differential area element in this region. The region $U(t)$ is determined by a chosen initial region $U(t_0)$, and defining $U(t)$ for all other times t by advecting $U(t_0)$ according to the flow map of the input field \mathbf{v} .

Average Killing field reference frame. From the representation of a Killing field via Eq. 8, if we have extracted a reference frame for each spatial point in a region of interest as above, we can simply take the average of all reference frames extracted in the region, by averaging each of the parameters a, b, c in Eq. 8 over the region, resulting in a single “average” Killing field. We note that this was also proposed and described in more detail by Zhang et al. [ZHTR22].

6 Using Local Reference Frames

Our use of *locally defined* reference frames has two major goals: (1) Discrete computation of space-time structures in a locally-adapted frame can increase the quality of the extracted structure significantly. (2) Visualizing space-time structures in a suitable frame reduces visual clutter and makes visualizations more natural and easy to interpret.

6.1 Explicit Reference Frame Transformations

We will need explicit expressions for the reference frame transformation ϕ_t , with the isometry according to Eq. 2, as well as the inverse transformation ϕ_t^{-1} , according to the isometry given by Eq. 6.

For $M = \mathbb{R}^2$, using Cartesian coordinates the rotation tensors $\mathbf{Q}(t)$ in Eqs. 2, 5, and 6 can be written using an angle function $\theta(t)$ as matrices

$$\mathbf{Q}(t) = \begin{bmatrix} \cos \theta(t) & -\sin \theta(t) \\ \sin \theta(t) & \cos \theta(t) \end{bmatrix}. \quad (22)$$

The world line $t \mapsto w(t)$ and the integrated angle $\theta(t)$, respectively, are the solutions of the respective ODEs

$$\frac{d}{dt} w(t) = \mathbf{w}(w(t), t), \quad \frac{d}{dt} \theta(t) = c(t). \quad (23)$$

Here, the angular velocity $c(t)$ is the single degree of freedom (for $M = \mathbb{R}^2$) that defines the spin tensor $\mathbf{\Omega}(t)$. By a well-known property of Killing fields in \mathbb{R}^n , both the curl of the field \mathbf{w} and the spin tensor $\mathbf{\Omega}(t)$ will be the same at every point of the domain \mathbb{R}^2 ,

and we have

$$\mathbf{\Omega}(t) = \begin{bmatrix} 0 & -c(t) \\ c(t) & 0 \end{bmatrix}. \quad (24)$$

The angular velocity $c(t)$ could be computed via the curl $\nabla \times$ as

$$c(t) := \frac{1}{2} \|\nabla \times \mathbf{w}\|. \quad (25)$$

However, from Eq. 8 with the basis Killing fields \mathbf{e}_i given in App. ??, we can see that the $c(t)$ in Eq. 8 and in Eqs. 24 and 25 are identical.

We can now solve the two ODEs in Eq. 23 above as the initial value problem (IVP) with $w(t_0)$ as chosen and $\theta(t_0) = 0$, giving

$$w(t) = w(t_0) + \int_{t_0}^t \mathbf{w}(w(\tau), \tau) d\tau, \quad \theta(t) = \int_{t_0}^t c(\tau) d\tau. \quad (26)$$

Space-time integration. In order to allow the user to interactively choose any time t_0 as a “reference time” for the visualization of space-time structures, we correspondingly integrate $w(t)$ and $\mathbf{Q}(t)$ in *both* time directions (forward and backward), starting from the interactively chosen, but otherwise arbitrary, time t_0 and $w(t_0)$, together with initial value $\theta(t_0) = 0$, immediately also giving $\mathbf{Q}(t_0) = \mathbf{I}$ (identity) via Eq. 22.

6.2 Structure Extraction

A key advantage of our framework is that for the extraction of structures we can use unmodified standard algorithms and implementations, for example as implemented in VTK or ParaView. In order to facilitate this approach, we (1) transform the input field using our reference frame transformation (Sec. A) before feature extraction. While this requires computing the transformed field across the entire domain, we demonstrate reduced overall computation time compared to direct extraction in the original frame. (2) apply the inverse transformation to extracted features (typically triangle meshes) to bring them back to the original frame. This lightweight post-processing is easily parallelizable and suitable for GPU acceleration. For implementation, we employ VTK’s marching cubes for iso-surfaces and Sadlo & Peikert’s Filtered AMR Ridge Extraction [SP07] for ridge extraction.

6.3 Reference Frame Aware Visualization

Visualizing objective structures in a local reference frame, which is usually not the input (lab) frame, aids detailed visual analysis. Coherent structures that are moving through space over time tend to become “vertical” in space-time visualizations in a reference frame that co-moves with them. See, Figs. 4 and 5 for examples. Fig. 10 in Appendix B illustrates the seeding of path lines in space-time in order to investigate the relationship between particle trajectories and (potential) material boundaries. In such visualizations it becomes better visible whether particles cross surfaces, which might necessitate further investigations whether these surfaces can in fact represent material boundaries.

In purely spatial visualizations (i.e., not space-time) structures look almost steady, i.e., almost not moving, instead of moving through the spatial domain. This allows for a visual analysis of the shape and how the shape of the structure changes over time. For example, in Fig. 5 and in the supplementary video we show iso-contours that merge and split over time, which is only easily visible

in the co-moving reference frame and much harder to observe in the lab reference frame.

7 Results and Discussion

In Fig. 1, we show material boundaries of a vortex street computed as FTLE ridges in $(2+1)$ -D space-time using ParaView. FTLE is a common tool in the visualization of material boundaries, and ridges of the FTLE field can be extracted to obtain a geometric representation of the boundary. We show a comparison of material boundaries, extracted in the local reference frame (Fig. 1 top), versus the lab reference frame (Fig. 1 bottom). The material boundary extraction in the local reference frame results in a smoother surface and reduced computation times (Table 1, *Cylinder-ridge*).

Temporal under-sampling. Fig. 3 illustrates the problem of temporal under-sampling in the original reference frame because of the fast motion of the vortex and the fine detail of the flow features. Using a reference frame that co-moves with the features can prevent temporal under-sampling in these scenarios. Fig. 3 (a) shows the synthetic data set. We compute the synthetic vortex structure that translates with increasing translational velocity by applying an unsteady reference frame translation $\mathbf{u}(x, y, t)$ to a steady vortex $\mathbf{v}(x, y)$ given as:

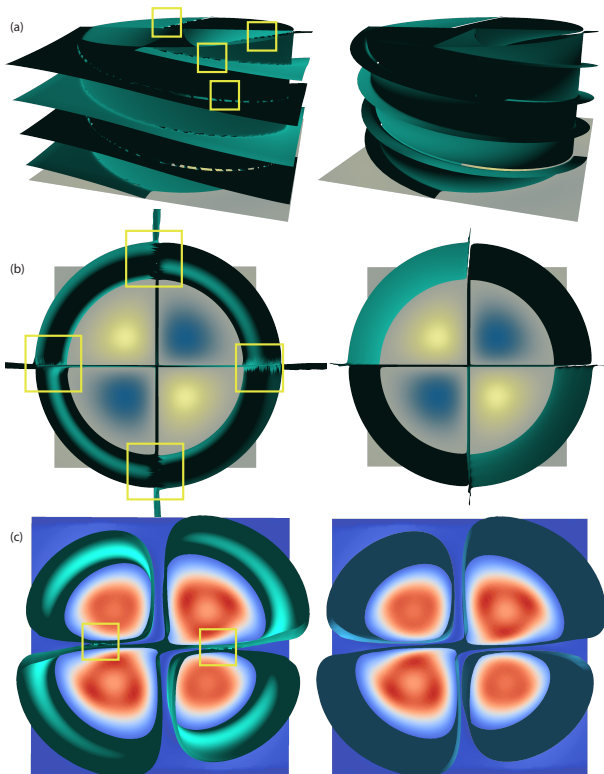


Figure 4: Removing Topological Defects. (a-c) Geometric and topological defects of potential material boundaries in the Four Centers synthetic flow when extracted in the input (lab) frame (left); no defects when extracted in local reference frame (right). (a-b) vorticity (non-objective), (c) Rotational component of Cauchy Green Deformation Tensor (objective).

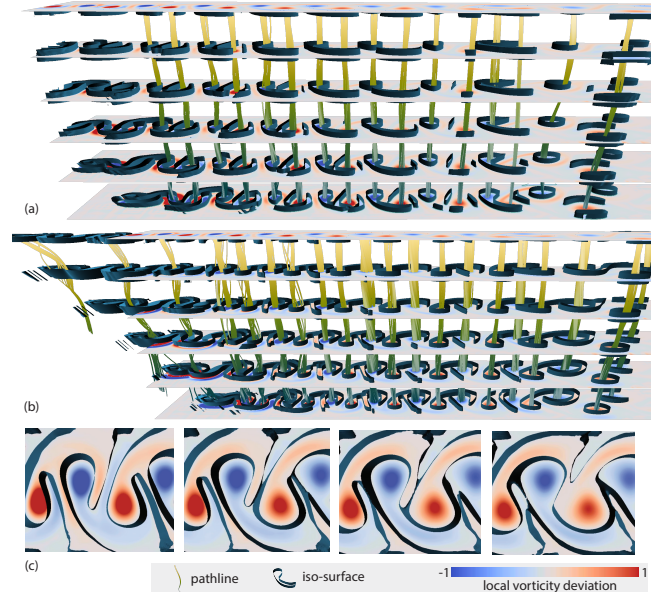


Figure 5: Local vorticity deviation iso-surfaces shown in a local reference frame: (a) Negative local vorticity deviation (iso-value: -0.1). (b) Positive local vorticity deviation (iso-value: 0.1). (c) Close-up of merging material boundary time-series (left to right, iso-value: 0).

$$\mathbf{v}(x, y) = \begin{pmatrix} -10ye^{-10((x+1)^2+y^2)} \\ 10(x+1)e^{-10((x+1)^2+y^2)} \end{pmatrix} \quad \mathbf{u}(x, y, t) = \begin{pmatrix} -0.25t \\ 0 \end{pmatrix}$$

We sample the synthetic vortex in the domain $x = [-4..4]$, $y = [-2..2]$ on a regular grid of size 256×128 . We sample the time domain $t = [0..5]$ at 32 equally spaced time steps. In Fig. 3 (b), we compare the extracted iso-surfaces visualized in the local reference frame of the feature. In Fig. 3 (c), we compare the extracted iso-surfaces visualized in the lab reference frame. Temporal under-sampling becomes a problem when features move too fast relative to the reference frame and when fine geometric details need to be resolved.

This result illustrates the meaning of Equation 18: Although in theory the extracted features are invariant to reference frame transformations, when discretely computing surfaces using standard software tools the reference frame does make a difference. Computing features in the local reference frame results in better quality because the local reference frame is best adapted to the feature.

One assumption that we make in our approach is that a suitable local reference frame exists and can be computed. While there are no guarantees for this in general, we have found that in many cases and potential application scenarios suitable local reference frames exist and can be extracted. In this paper we treat the computation of observer fields as a black-box, since different methods for the numerical optimization exist [GGT17, HMTR19, RMB*21, RZW*24]. In principle, our method is agnostic to the method that defines the observer motion. Notably, numerical optimization methods are not the only way to define observer fields. In certain application scenarios, an observer motion can even be assumed or inferred from simulation parameters. Since reference frame transformations do

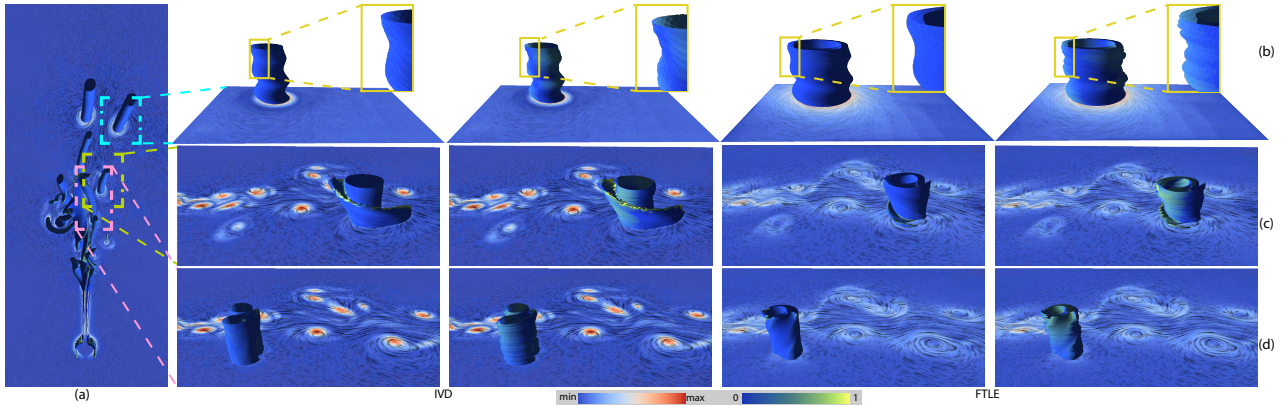


Figure 6: Comparing material boundaries in local reference frames. Iso-surfaces of IVD and FTLE (IVD and FTLE color-coded on the plane: blue to red). (a) overview of dataset. (b) Crop out of region 1. (c) Crop out of region 2. (d) Crop out of region 3. (b,c,d) surface complexity visualized in the local reference frame, from left to right: IVD (ours), IVD (original frame), FTLE (ours), FTLE (original frame). Note that the surface curvature (color-coding blue to yellow) is only lower in the time-direction when computed in the local reference frame.

not affect the correctness of the solution, they can be applied in the reference frame that is found to be most suitable and leads to the least topological artifacts in practice.

7.1 Interactively Changing Local Reference Frames

Fig. 6 demonstrates the effectiveness of our technique by comparing material boundaries extracted in both the original and local reference frames. Specifically, it showcases iso-surfaces of the Instantaneous Vorticity Deviation (IVD) and the Finite-Time Lyapunov Exponent (FTLE). Panel (a) provides an overview of the dataset, while panels (b), (c), and (d) present cropped regions. In these cropped views, the surfaces are arranged from left to right as follows: IVD computed using our method, IVD in the original frame, FTLE with our method, and FTLE in the original frame. The surfaces are color-coded from blue to yellow to represent curvature.

A key observation from the figure is that the iso-surfaces computed in the local reference frame exhibit significantly lower curvature in the time direction compared to those in the original frame. This reduction in curvature indicates that the extracted local reference frame effectively makes the flow features as steady as possible. Importantly, this improvement is achieved by employing rigid motion observers, ensuring that the reference frame transformation remains physically correct and interpretable.

The reduced geometric complexity—evident from lower triangle counts (see Table 1) and decreased curvature in the time direction—is not the result of simply smoothing out the geometry. Instead, it stems from adopting a physical observer that optimally co-moves with the flow structures. As a consequence, the curvature and fidelity of the surfaces are not smoothed in space but are optimally adjusted over the time dimension. This leads to better visualizations that enhance the representation of flow features without compromising their physical accuracy.

The computation of material boundaries in the local reference frame of a moving feature opens the door for a novel interactive visualization tool. We can interactively extract iso-contour components at a location chosen by the user. Since iso-contour extraction is much faster than iso-surface extraction we can repeat this procedure in several time steps by following the reference frame. This effec-

tively provides a preview of the iso-surface. Without a suitable local reference frame it is not possible to consistently choose the correct iso-surface component over time. Fig. 8 in Appendix B shows two iso-contour previews with the resulting iso-surfaces. The supplementary video demonstrates how this novel interactive method is used in the exploration of a dataset.

7.2 Evolution of Boundaries in the Local Reference Frame

In Fig. 5, we show a simulated von Kármán vortex street. In this case study, we demonstrate the visualization of material boundaries delineating areas of clockwise and anti-clockwise rotation. By using a local reference frame that moves alongside the evolving vortex street, we are able to capture the dynamic development of these separating boundaries over time. We extract iso-surfaces from the scalar field of local vorticity deviation, which has been calculated relative to the co-moving reference frame. Figs. 5 (a) and (b) are space-time visualizations with the time dimension as the vertical axis. We show time-slices of the iso-surfaces with iso-values (a) -0.1 and (b) 0.1 . Path lines of particles show a good agreement of the clockwise and counter-clockwise separating boundaries. In Fig. 5 (c), we show a time-series of the evolution of the iso-surface boundary with iso-value 0 . The perspective of the co-moving reference frame allows for an in-depth analysis of the material boundary over time. Notably, in this reference frame we can observe how these boundaries, which remain stable for some time, converge and merge during later stages of the evolution of the vortex street. See the video in the supplementary material for an interactive visualization of the evolution of boundaries that is much easier to observe in the local reference frame.

7.3 Topological Artifact Removal in the Local Reference Frame

In Fig. 4 we show a case-study of investigating the material boundaries of the synthetic four centers vector field. In Fig. 4 (a-c) on the left side we highlight geometric and topological defects that are introduced by extraction operators that operate in the lab reference frame and compare to our method that extracts iso-surfaces in the local reference frame.

In Fig. 4 (a), we show that the visualization of potential material

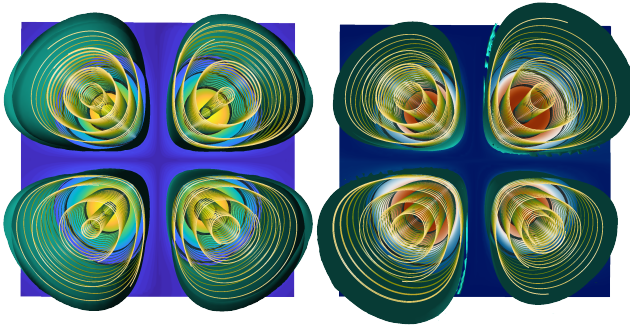


Figure 7: Investigating material boundaries. Material boundaries extracted in a local reference frame. Path lines confirm the close match between both material boundaries and their contained particles. Left: LAVD and right: Lagrangian of the rotational component of the Cauchy-Green Deformation Tensor

boundaries in the lab-frame prevents us from understanding the structure of the flow field, while in (b) when visualizing the same geometry in the local reference frame of the features, the potential material boundaries become apparent.

In Fig. 4 (c), we show an objective invariant of the Cauchy-Green deformation tensor. We consider the rotational component of the Cauchy-Green deformation tensor that results in objective material boundary candidates. The topological defects on the left in Fig. 4 (c) lead to the extraction of a single iso-surface component. The topological defects are removed on the right in Fig. 4 (c) resulting in three distinct iso-surfaces.

Although the defects in Fig. 4 (a-c) appear to be small, they alter the topology of the surface, wrongly fusing independent components of the boundary. Defects like these can significantly complicate the analysis and further processing of boundaries.

7.4 Lagrangian Structures in the Local Reference Frame

We show the use of our visualization method to compare existing and to design new Lagrangian Structure extraction methods. In Fig. 7 we show the use of our visualization tool to compare results from the well established LAVD method on the left - which integrates the vorticity deviation along particle trajectories - and on the right we show a new method which integrates the rotational component of the Cauchy-Green deformation tensor (shown in Fig 4 (c)). Both Lagrangian Structures in Fig. 7 are extracted from objective tensor fields and show perfect agreement with the path lines of the particles that are contained inside the boundary.

A key result of our research is the application of our method to extract and analyze material boundary candidates in the local reference frame. In Appendix B Fig. 10 we show a comparison of material boundary candidates derived from multiple vortex region methods. Our method allows to visualize the superior accuracy of the LAVD method in aligning boundaries with path line trajectories, in this idealized model of a simplified model used to study geophysical fluid dynamics.

Table 1 summarizes the performance measurements comparing iso-, and ridge-surface extraction in the Original Reference Frame (Ext-ORF) with our proposed method in the Local Reference Frame (Total-LRF), which consists of a scalar field transformation (S-RTF)

| Dataset | Res | Tri-ORF | Tri-LRF | Ext-ORF [s] | (S-RFT [s] | + Ext-LRF [s] | = Total-LRF [s] |
|------------------|--------------|---------|---------|-------------|------------|---------------|-----------------|
| RFC | 512x512x128 | 2984K | 887K | 8.81 | 0.17 | 2.49 | 2.66 |
| RFC | 128x128x32 | 287K | 68K | 0.92 | 0.01 | 0.15 | 0.16 |
| Boussinesq-iso-1 | 256x512x150 | 278K | 120K | 1.02 | 0.15 | 0.48 | 0.63 |
| Boussinesq-iso-2 | 256x256x150 | 474K | 209K | 1.25 | 0.07 | 0.62 | 0.69 |
| Boussinesq-iso-3 | 64x128x150 | 118K | 78K | 0.38 | 0.01 | 0.22 | 0.23 |
| Boussinesq-iso-4 | 512x1024x150 | 108K | 76K | 1.90 | 0.61 | 1.22 | 1.83 |
| Bickley Jet | 2048x256x300 | 194K | 94K | 2.46 | 0.83 | 0.96 | 1.79 |
| Cylinder-iso | 1024x512x256 | 24851K | 1426K | 12.40 | 1.21 | 5.41 | 6.62 |
| Cylinder-ridge | 1280x160x32 | 6406K | 3359K | 268.48 | 0.21 | 175.67 | 175.88 |

Table 1: Performance comparison of extracting surfaces in the Original Reference Frame (Ext-ORF) and in the Local Reference Frame (Total-LRF). All time measurements are in seconds. Res is the resolution of the input scalar field. S-RFT is the time to compute the reference frame transformation of the scalar field. The triangle count is reported for the surfaces in the Original Reference Frame (Tri-ORF) and in the Local Reference Frame (Tri-LRF). The lower geometric complexity of the extracted surfaces in the local reference frame leads to faster computation times, also compensating for the overhead of the reference transformation of the scalar field.

followed by the surface extraction (Ext-LRF). Although our method introduces an additional computation step (the scalar field reference frame transformation), the total computation time (Total-LRF) is lower than that of the traditional approach. This efficiency gain is due to the significantly reduced geometric complexity of the surfaces in the local reference frame, as indicated by the lower triangle count (Tri-LRF) compared to the number of triangles in the original reference frame (Tri-ORF). Since the computational cost is dominated by the surface extraction process, the simpler geometry in the local reference frame leads to faster computations, which compensates for the overhead of the transformation step. Consequently, our method not only produces iso-, and ridge-surfaces with enhanced geometric and topological fidelity, but also achieves a reduction in total computation time.

8 Conclusions

In this paper, we have presented a general framework that proposes to both *compute* as well as *visualize* coherent structures, such as material boundaries, in a local reference frame. The resulting visualizations often exhibit reduced visual clutter, which can greatly facilitate interactive exploration and analysis. Moreover, even if a standard visualization in the original input (lab) reference frame is desired, we have shown that computing the structures of interest in the local reference frame and then transforming the result back to the input frame can lead to quality improvements and remove topological artifacts due reduced issues with discretization and sampling in the time domain. Further, we have demonstrated the computational efficiency of our approach and introduced a novel interactive iso-contour component preview visualization that is enabled by local reference frames. We believe that in addition to the existing great variety of powerful feature-adaptive computation approaches, it is very beneficial to also offer interactive visualization and exploration capabilities that fully take reference frame transformations into account. Ultimately, the concept of interactively choosing and changing the reference frame which is used for the visualization, and computation of features as proposed here, could become an important ingredient of visual analysis software for fluid flows.

Acknowledgments

This work was supported by King Abdullah University of Science and Technology (KAUST) baseline funding. This research used resources of the Core Labs of KAUST.

References

- [AGL05] AHRENS J., GEVECI B., LAW C.: Paraview: An end-user tool for large data visualization. *Visualization Handbook* (01 2005). 2
- [Ast79] ASTARITA G.: Objective and generally applicable criteria for flow classification. *Journal of Non-Newtonian Fluid Mechanics* 6, 1 (1979), 69–76. doi:10.1016/0377-0257(79)87004-4. 2
- [BCG20] BERENJKOUB M., CHEN G., GÜNTHER T.: Vortex boundary identification using convolutional neural network. In *IEEE VIS 2020 Short Papers* (2020), pp. 261–265. doi:10.1109/VIS47514.2020.00059. 3
- [BHJ16] BUJACK R., HLAWITSCHKA M., JOY K. I.: Topology-inspired Galilean invariant vector field analysis. In *Proceedings of IEEE Pacific Visualization 2016* (2016), pp. 72–79. doi:10.1109/PACIFICVIS.2016.7465253. 2
- [BMBF*19] BIN MASOOD T., BUDIN J., FALK M., FAVELIER G., GARTH C., GUEUNET C., GUILLOU P., HOFMANN L., HRISTOV P., KAMAKSHIDASAN A., KAPPE C., KLACANSKY P., LAURIN P., LEVINE J., LUKASCZYK J., SAKURAI D., SOLER M., STENETEG P., TIERNY J., USHER W., VIDAL J., WOZNIAC M.: An Overview of the Topology ToolKit. In *TopoInVis* (2019). 2
- [BP02] BAUER D., PEIKERT R.: Vortex Tracking in Scale-Space. In *Proceedings of Eurographics/IEEE TCVG Symposium on Visualization 2002* (2002), pp. 233–241. doi:10.2312/VisSym/VisSym02/233-240. 3
- [BPKB14] BHATIA H., PASCUCCI V., KIRBY R. M., BREMER P.-T.: Extracting features from time-dependent vector fields using internal reference frames. *Computer Graphics Forum* 33, 3 (2014), 21–30. doi:10.1111/cgf.12358. 3
- [BRG20] BAEZA ROJO I., GÜNTHER T.: Vector field topology of time-dependent flows in a steady reference frame. *IEEE Transactions on Visualization and Computer Graphics* 26, 1 (2020), 280–290. doi:10.1109/TVCG.2019.2934375. 2
- [BS95] BANKS D. C., SINGER B. A.: A predictor-corrector technique for visualizing unsteady flow. 151–163. doi:10.1109/2945.468404. 3
- [BYH*20] BUJACK R., YAN L., HOTZ I., GARTH C., WANG B.: State of the art in time-dependent flow topology: Interpreting physical meaningfulness through mathematical properties. *Computer Graphics Forum* 39, 3 (2020), 811–835. doi:10.1111/cgf.14037. 3
- [DL76] DROUOT R., LUCIUS M.: Approximation du second ordre de la loi de comportement des fluides simples. lois classiques déduites de l'introduction d'un nouveau tenseur objectif. *Archivum Mechaniki Stosowanej* 28, 2 (1976), 189–198. 2
- [FP01] FURST J. D., PIZER S. M.: Marching ridges. In *IASTED International Conference on Signal and Image Processing* (2001), pp. 22–26. 2
- [GGT17] GÜNTHER T., GROSS M., THEISEL H.: Generic objective vortices for flow visualization. *ACM Transactions on Graphics* 36, 4 (July 2017). URL: <https://doi.org/10.1145/3072959.3073684>, doi:10.1145/3072959.3073684. 2, 6, 8
- [GLL91] GLOBUS A., LEVIT C., LASINSKI T.: A tool for visualizing the topology of three-dimensional vector fields. In *Proceedings of IEEE Visualization 1991* (1991), pp. 33–40. doi:10.1109/VISUAL.1991.175773. 3
- [GLX*21] GUO H., LENZ D., XU J., LIANG X., HE W., GRINDEANU I. R., SHEN H.-W., PETERKA T., MUNSON T., FOSTER I.: Ftk: A simplicial spacetime meshing framework for robust and scalable feature tracking. *IEEE Transactions on Visualization and Computer Graphics* 27, 8 (Aug. 2021), 3463–3480. URL: <http://dx.doi.org/10.1109/TVCG.2021.3073399>, doi:10.1109/tvcg.2021.3073399. 2
- [GST16] GÜNTHER T., SCHULZE M., THEISEL H.: Rotation invariant vortices for flow visualization. *IEEE Transactions on Visualization and Computer Graphics* 22, 1 (2016), 817–826. doi:10.1109/TVCG.2015.2467200. 2
- [GT18] GÜNTHER T., THEISEL H.: The state of the art in vortex extraction. *Computer Graphics Forum* 37, 6 (2018), 149–173. doi:10.1111/cgf.13319. 3
- [GT20] GÜNTHER T., THEISEL H.: Hyper-objective vortices. *IEEE Transactions on Visualization and Computer Graphics* 26, 3 (2020), 1532–1547. doi:10.1109/TVCG.2018.2868760. 2
- [Hal01] HALLER G.: Distinguished material surfaces and coherent structures in three-dimensional fluid flows. *Physica D: Nonlinear Phenomena* 149, 4 (2001), 248–277. doi:10.1016/S0167-2789(00)00199-8. 2, 5
- [Hal05] HALLER G.: An objective definition of a vortex. *Journal of Fluid Mechanics* 525 (2005), 1–26. doi:10.1017/S0022112004002526. 2
- [Hal15] HALLER G.: Lagrangian coherent structures. *Annual Review of Fluid Mechanics* 47, 1 (Jan. 2015), 137–162. URL: <http://dx.doi.org/10.1146/annurev-fluid-010313-141322>, doi:10.1146/annurev-fluid-010313-141322. 1, 2, 5
- [HHFH16] HALLER G., HADJIGHASEM A., FARAZMAND M., HUHNF.: Defining coherent vortices objectively from the vorticity. *Journal of Fluid Mechanics* 795 (2016), 136–173. doi:10.1017/jfm.2016.151. 2, 3, 5
- [HMR19] HADWIGER M., MLEJNEK M., THEUSSL T., RAUTEK P.: Time-dependent flow seen through approximate observer killing fields. *IEEE Transactions on Visualization and Computer Graphics* 25, 1 (2019), 1257–1266. doi:10.1109/TVCG.2018.2864839. 2, 3, 6, 8
- [HS20] HOFMANN L., SADLO F.: Extraction of distinguished hyperbolic trajectories for 2d time-dependent vector field topology. *Computer Graphics Forum* 39, 3 (2020), 303–315. doi:10.1111/cgf.13982. 2
- [HWM88] HUNT J. C. R., WRAY A. A., MOIN P.: Eddies, streams, and convergence zones in turbulent flows. In *Proceedings of the Summer Program 1988* (Dec. 1988), Center for Turbulence Research, pp. 193–208. 3
- [HY00] HALLER G., YUAN G.: Lagrangian coherent structures and mixing in two-dimensional turbulence. *Physica D: Nonlinear Phenomena* 147, 3–4 (Dec. 2000), 352–370. URL: [http://dx.doi.org/10.1016/S0167-2789\(00\)00142-1](http://dx.doi.org/10.1016/S0167-2789(00)00142-1), doi:10.1016/S0167-2789(00)00142-1. 1, 2, 5
- [JH95] JEONG J., HUSSAIN F.: On the identification of a vortex. *Journal of Fluid Mechanics* 285 (1995), 69–94. doi:10.1017/S0022112095000462. 3
- [JW02] JONES C., WINKLER S.: Invariant manifolds and lagrangian dynamics in the ocean and atmosphere. In *Handbook of Dynamical Systems*, Fiedler B., (Ed.). Springer, 2002, pp. 55–92. doi:10.1016/S1874-575X(02)80023-6. 2
- [KG19] KIM B., GÜNTHER T.: Robust reference frame extraction from unsteady 2d vector fields with convolutional neural networks. *Computer Graphics Forum* 38, 3 (2019), 285–295. doi:10.1111/cgf.13689. 3
- [Kit03] KITWARE, INC.: *The Visualization Toolkit user's guide*, Jan. 2003. URL: <http://www.kitware.com/publications/item/view/1269>. 2
- [KPH22] KASZÁS B., PEDERGNANA T., HALLER G.: The objective deformation component of a velocity field. *European Journal of Mechanics - B/Fluids* (2022). URL: <https://www.sciencedirect.com/science/article/pii/S0997754622001571>, doi:10.1016/j.euromechflu.2022.12.007. 3, 4, 6, 7
- [KRHH11] KASTEN J., REININGHAUS J., HOTZ I., HEGE H.-C.: Two-dimensional time-dependent vortex regions based on the acceleration magnitude. *IEEE Transactions on Visualization and Computer Graphics* 17, 12 (2011), 2080–2087. doi:10.1109/TVCG.2011.249. 3
- [KWP*10] KASTEN J., WEINKAUF T., PETZ C., HOTZ I., NOACK B. R., HEGE H.-C.: *Extraction of Coherent Structures from Natural and Actuated Flows*. Springer Berlin Heidelberg, 2010, p. 373–387. URL:

- http://dx.doi.org/10.1007/978-3-642-11735-0_24, doi:10.1007/978-3-642-11735-0_24. 2
- [Lug79] LUGT H. J.: The dilemma of defining a vortex. In *Recent developments in theoretical and experimental fluid mechanics*. Springer, 1979, pp. 309–321. doi:10.1007/978-3-642-67220-0_32. 2
- [Ogd97] OGDEN R. W.: *Non-Linear Elastic Deformations*. Dover Publications, Inc., 1997. 2
- [Oku70] OKUBO A.: Horizontal dispersion of floatable particles in the vicinity of velocity singularities such as convergences. *Deep Sea Research and Oceanographic Abstracts* 17, 3 (June 1970), 445–454. doi:10.1016/0011-7471(70)90059-8. 3
- [O'N06] O'NEILL B.: *Elementary Differential Geometry*, revised 2nd ed. Academic Press, 2006. 4
- [PC87] PERRY A. E., CHONG M. S.: A description of eddying motions and flow patterns using critical-point concepts. *Ann. Rev. Fluid Mech.* 19, 1 (1987), 125–155. doi:10.1146/annurev.fl.19.010187.001013. 2
- [PC94] PERRY A. E., CHONG M. S.: Topology of flow patterns in vortex motions and turbulence. *Applied Scientific Research* 53, 3 (1994), 357–374. doi:10.1007/bf00849110. 2
- [PPF*10] POBITZER A., PEIKERT R., FUCHS R., SCHINDLER B., KUHN A., THEISEL H., MATKOVIC K., HAUSER H.: On the way towards topology-based visualization of unsteady flow, 2010. URL: <https://diglib.eg.org/handle/10.2312/egst.20101065.137-154>, doi:10.2312/EGST.20101065. 2
- [PR99] PEIKERT R., ROTH M.: The "Parallel Vectors" operator—a vector field visualization primitive. In *Proceedings of IEEE Visualization 1999* (1999), pp. 263–532. doi:10.1109/visual.1999.809896. 3
- [PVH*03] POST F. H., VROLIJK B., HAUSER H., LARAMEE R. S., DOLEISCH H.: The state of the art in flow visualisation: Feature extraction and tracking. *Computer Graphics Forum* 22, 4 (2003), 775–792. doi:10.1111/j.1467-8659.2003.00723.x. 2
- [RG23] REN C., GUO H.: Meshing deforming spacetime for visualization and analysis. In *arXiv preprint arXiv:2309.02677* (2023). doi:10.48550/arXiv.2309.02677. 2
- [RMB*21] RAUTEK P., MLEJNEK M., BEYER J., TROIDL J., PFISTER H., THEUSSL T., HADWIGER M.: Objective observer-relative flow visualization in curved spaces for unsteady 2D geophysical flows. *IEEE Transactions on Visualization and Computer Graphics (Proceedings IEEE Scientific Visualization 2020)* 27, 2 (2021), 283–293. doi:10.1109/TVCG.2020.3030454. 2, 6, 8
- [RZW*24] RAUTEK P., ZHANG X., WOSCHIZKA B., THEUSSL T., HADWIGER M.: Vortex lens: Interactive vortex core line extraction using observed line integral convolution. *IEEE Transactions on Visualization and Computer Graphics (Proceedings IEEE Scientific Visualization 2023)* 30, 1 (2024), 55–65. doi:10.1109/TVCG.2023.3326915. 2, 4, 6, 7, 8
- [Ser17] SERRA M.: *A Geometric Approach to Coherent Structures in Complex Dynamical Systems*. PhD thesis, ETH Zürich, 2017. 2, 5
- [SH95] SUJUDI D., HAIMES R.: Identification of swirling flow in 3-d vector fields. In *Proceedings of the 12th Computational Fluid Dynamics Conference* (1995), pp. 792–799. doi:10.2514/6.1995-1715. 3
- [SHH*19] SADLO F., HAUSNER P., HOFMANN L., JUNG P., KARCH G., PEIKERT R., PILZ L., ROTH M., SDEO K.: VCG ParaView plugins, March 2019. URL: <https://vcg.iwr.uni-heidelberg.de/plugins/>. 2
- [SLM05] SHADDEN S. C., LEKIEN F., MARSDEN J. E.: Definition and properties of lagrangian coherent structures from finite-time Lyapunov exponents in two-dimensional aperiodic flows. *Physica D: Nonlinear Phenomena* 212, 3 (2005), 271–304. doi:10.1016/j.physd.2005.10.007. 2, 5
- [SML06] SCHROEDER W., MARTIN K., LORENSEN W.: *The Visualization Toolkit, An Object-Oriented Approach To 3D Graphics*, 4th ed. 2006. 2
- [SP07] SADLO F., PEIKERT R.: Efficient visualization of lagrangian coherent structures by filtered amr ridge extraction. *IEEE transactions on visualization and computer graphics* 13, 6 (2007), 1456–1463. 7
- [SP09] SADLO F., PEIKERT R.: Visualizing lagrangian coherent structures and comparison to vector field topology. In *Topology-Based Methods in Visualization II*, Hege H.-C., Polthier K., Scheuermann G., (Eds.). Springer Berlin Heidelberg, 2009, pp. 15–29. URL: <https://doi.org/10.1007/978-3-540-88606-8%5F2>, doi:10.1007/978-3-540-88606-8_2. 2
- [SPP04] SADLO F., PEIKERT R., PARKINSON E.: Vorticity based flow analysis and visualization for pelton turbine design optimization. In *Proceedings of IEEE Visualization 2004* (2004), pp. 179–186. doi:10.1109/visual.2004.128. 3
- [SWH05] SAHNER J., WEINKAUF T., HEGE H.-C.: Galilean Invariant Extraction and Iconic Representation of Vortex Core Lines. In *EUROVIS 2005: Eurographics / IEEE VGTC Symposium on Visualization* (2005), Brodlie K., Duke D., Joy K., (Eds.), The Eurographics Association, pp. 151–160. doi:10.2312/VisSym/EuroVis05/151-160. 2
- [TFL*17] TIERNY J., FAVELIER G., LEVINE J. A., GUEUNET C., MICHAUX M.: The Topology ToolKit. *IEEE Transactions on Visualization and Computer Graphics (Proc. of IEEE VIS)* (2017). URL: <https://topology-tool-kit.github.io/>. 2
- [THR*21] THEISEL H., HADWIGER M., RAUTEK P., THEUSSL T., GÜNTHER T.: Vortex criteria can be objectivized by unsteadiness minimization. *Physics of Fluids* 33, 10 (2021), 107115. doi:10.1063/5.0063817. 2
- [TN65] TRUESDELL C., NOLL W.: *The Nonlinear Field Theories of Mechanics*. Springer, 1965. 2
- [TS03] THEISEL H., SEIDEL H.-P.: Feature flow fields. In *Proc. Joint Eurographics - IEEE TCVC Symposium on Visualization (VisSym'03)* (2003), Bonneau G.-P., Hahmann S., (Ed.) C. H., (Eds.), pp. 141–148. 2, 3
- [TWH05] THEISEL H., WEINKAUF T., HEGE H.-C., SEIDEL H.-P.: Topological methods for 2d time-dependent vector fields based on stream lines and path lines. *IEEE Transactions on Visualization and Computer Graphics* 11, 4 (2005), 383–394. doi:10.1109/TVCG.2005.68. 3
- [TWSH02] TRICOCHÉ X., WISCHGOLL T., SCHEUERMANN G., HAGEN H.: Topology tracking for the visualization of time-dependent two-dimensional flows. *Computers & Graphics* 26, 2 (2002), 249–257. doi:10.1016/s0097-8493(02)00056-0. 3
- [WCW*09] WIEBEL A., CHAN R., WOLF C., ROBITZKI A., STEVENS A., SCHEUERMANN G.: Topological flow structures in a mathematical model for rotation-mediated cell aggregation. In *Topological Methods in Data Analysis and Visualization, Mathematics and Visualization* (2009), pp. 193–204. doi:10.1007/978-3-642-15014-2_16. 3
- [Wei91] WEISS J.: The dynamics of enstrophy transfer in two-dimensional hydrodynamics. *Physica D: Nonlinear Phenomena* 48, 2 (Mar. 1991), 273–294. doi:10.1016/0167-2789(91)90088-q. 3
- [WSTH07] WEINKAUF T., SAHNER J., THEISEL H., HEGE H.-C.: Cores of swirling particle motion in unsteady flows. *IEEE Transactions on Visualization and Computer Graphics (Proc. IEEE Visualization)* 13, 6 (2007), 1759–1766. doi:10.1109/TVCG.2007.70545. 2
- [XXLL10] XIE C., XING L., LIU C., LI X.: Multi-scale vortex extraction of ocean flow. In *Visual Information Communication*, Huang M. L., (Ed.). Springer-Verlag, 2010, pp. 173–183. doi:10.1007/978-1-4419-0312-9_11. 3
- [ZHTR22] ZHANG X., HADWIGER M., THEUSSL T., RAUTEK P.: Interactive exploration of physically-observable objective vortices in unsteady 2D flow. *IEEE Transactions on Visualization and Computer Graphics* 28, 1 (2022), 281–290. URL: <https://doi.org/10.1109/TVCG.2021.3115565>, doi:10.1109/TVCG.2021.3115565. 2, 3, 4, 6, 7